PAPER

Defective Ce–Mn solid solution loaded with Pd single atoms for an enhanced methane combustion reaction†

Haoyang Liu,[a,b] Huilin Wang,*[a,b] Xiang Chu,[a,b] Zijian Wang,[a,b] Yuou Li,[a,b] Shibo Zhang,[a,b] Xiao Wang,*[a,b] Zhenan Qiao, [c] Shuyan Song [*a,b] and Hongjie Zhang [a,b,d]

Methane combustion reactions hold significant promise for addressing environmental issues, particularly the greenhouse effect attributed to anthropogenic emissions. However, current catalysts face challenges in simultaneously achieving low-temperature activity and high-temperature stability. In this work, a CeMn solid solution decorated with palladium single atoms (Pd/CeMn-AR) was synthesized *via* a one-pot auto-redox method. Experimental findings indicate that the Pd/CeMn-AR catalyst demonstrates favorable activity and stability in the methane oxidation reaction. Specifically, the T_{90} of Pd/CeMn-AR reaches 543 °C, significantly better than its Pd/CeO$_2$ (627 °C), Pd/MnO$_x$ (634 °C) and Pd/CeMn-CP (557 °C) counterparts. Furthermore, after 10 hours of continuous reaction at elevated temperatures of 550 °C and 650 °C, the Pd/CeMn-AR catalyst retains more than 95% of its initial activity. Mechanistic investigations reveal that the autoxidative synthesis strategy enhances the exposure of oxygen vacancies, promotes the adsorption of substrates, and accelerates the oxidative conversion of intermediates, ultimately improving the catalytic efficiency.

Introduction

Mitigating climate change and ecological disruptions stemming from the greenhouse effect poses a formidable global challenge.[1] Methane (CH$_4$) is the second most prominent greenhouse gas after CO$_2$, with a global warming potential of up to 25.[2–4] Hence, reducing the emission of CH$_4$ into the atmosphere is of great importance for sustainable human development.[5–7] The methane combustion reaction (CH$_4$ + O$_2$ → CO$_2$ + H$_2$O) provides a simple but efficient way to handle this issue. Compared to traditional methane combustion utilizing an open flame, the catalytic combustion process facilitates lower operational temperatures and generates fewer toxic byproducts, thereby emerging as a research focus in recent years.[8–12] Low-temperature catalytic activity and high-temperature thermal stability are the two most important performance indicators for catalytic methane combustion.[3,13–17] Benefiting from abundant d-band electron states, noble metal-based catalysts are favourable for activating methane molecules through σ-d interactions, showing superior low-temperature activity.[18] However, the harsh reaction conditions at high temperatures lead to agglomeration or decomposition of the loaded active centres, resulting in a significant loss of their initial activity.[4,19–21] Therefore, designing noble metal active centres that can accommodate both low and high temperatures requires revolutionary updates to the catalyst structure.[22,23]

Among the many precious metals, Pd-based catalysts are extensively researched and regarded as the most promising candidates for methane oxidation.[24–26] Identifying highly stable and active palladium nanostructures has consistently been the focus of research endeavors.[15] Wang's group reported the reversible transformation behaviour of Pd single atoms on CeO$_2$ across various stages of automotive exhaust aftertreatment.[27] The PdO$_x$ clusters reduced in a CO atmosphere exhibit enhanced low-temperature CH$_4$ oxidation activity. However, the redispersion of PdO$_x$ clusters into Pd atoms leads to a decline in conversion efficiency, severely constraining their potential applications. Considering that atomically dispersed Pd atoms are thermodynamically stable at high temperature, constructing highly active Pd single atoms offers a viable solution to the inevitable deactivation issues. A major challenge lies in efficiently accomplishing methane and oxygen

[a]State Key Laboratory of Rare Earth Resource Utilization, Changchun Institute of Applied Chemistry, Chinese Academy of Sciences, Changchun 130022, China. E-mail: wanghl@ciac.ac.cn, wangxiao@ciac.ac.cn, songsy@ciac.ac.cn
[b]University of Science and Technology of China, Hefei 230026, China
[c]State Key Laboratory of Inorganic Synthesis and Preparative Chemistry, College of Chemistry, Jilin University, Changchun 130012, China
[d]Department of Chemistry, Tsinghua University, Beijing 100084, China
†Electronic supplementary information (ESI) available: Figures of the characterization of the as-prepared catalysts. See DOI: https://doi.org/10.1039/d5dt00409h

activation on an individual Pd atom.[19] Unlike the direct supply of O by PdO_x particles, the O_2 activation process of a single-atom catalyst predominantly takes place on the support.[16] Xie's group introduced Rh atoms onto Pd_1/CeO_2 and improved the oxygen vacancy formation ability of CeO_2, while the CH_4 conversion was still less than 10% at 400 °C.[28] Wu's group synthesized a $Pd^{\delta+}$ ($0 < \delta < 2$) single site with an under-coordinated local structure, which exhibited a weak interaction with the ceria support. This enhanced the oxygen supply capacity of the support and decreased T_{50} to 450 °C.[24] Despite extensive efforts that have been made, there is still much room for improving the methane combustion performance of Pd/CeO_2 catalysts.[7]

Herein, we synthesized a multicomponent methane combustion catalyst consisting of CeMn solid solutions loaded with Pd single atoms (Pd/CeMn-AR) based on a modified auto-redox reaction, exhibiting superior low-temperature activity and high-temperature stability. Specifically, the T_{90} of Pd/CeMn-AR reaches 543 °C, significantly better than its Pd/CeO_2 (627 °C), Pd/MnO_x (634 °C) and Pd/CeMn-CP (557 °C) counterparts. Notably, Pd/CeMn-AR can maintain more than 95% of its initial activity at elevated temperatures of 550 °C and 650 °C after 10 hours of continuous reaction. Mechanistic studies revealed the crucial role of the one-pot auto-redox reaction synthesis strategy in generating abundant surface oxygen vacancies, which facilitates substrate adsorption and accelerates the oxidative conversion of CH_3^* intermediates.

Results and discussion

Material characterization

According to previous studies, Pd/CeMn-AR was synthesized by a one-pot auto-redox reaction involving Ce^{3+}, Pd^{2+}, and MnO_4^-, as illustrated in Fig. 1a.[29,30] We first study the morphology of the as-obtained catalyst by transmission electron microscopy (TEM). The low-magnification TEM image depicted in Fig. 1b reveals a nanosphere morphology composed of smaller nanoparticles. To identify the composition of the sample, aberration-corrected high-angle dark-field scanning transmission electron microscopy (HAADF-STEM) was conducted for a detailed structural observation. Fig. 1c displays measured lattice spacings of 0.32 nm and 0.28 nm, which correspond to the (111) and (200) planes of the CeMn solid solution, indicating that Ce and Mn are well fused. Meanwhile, some bright dots associated with Pd single atoms are observed, with no evidence of Pd nanoparticle formation. The corresponding energy dispersive X-ray spectroscopy (EDX) mapping images in Fig. 1d demonstrate a uniform distribution of Ce, Mn, Pd, and O elements, confirming the successful formation of nanosized solid solution and the atomically dispersed nature of Pd atoms. In addition, we have obtained a higher-resolution image of Pd/CeMn-AR by HAADF-STEM, as displayed in Fig. S1.† Enlargement of the yellow-boxed area in Fig. S1a† demonstrates bright spots corresponding to isolated Pd atoms, as confirmed by the strong peak at 400 pm from the X- to Y-axis in Fig. S1c.† It further demonstrates the atomic dis-
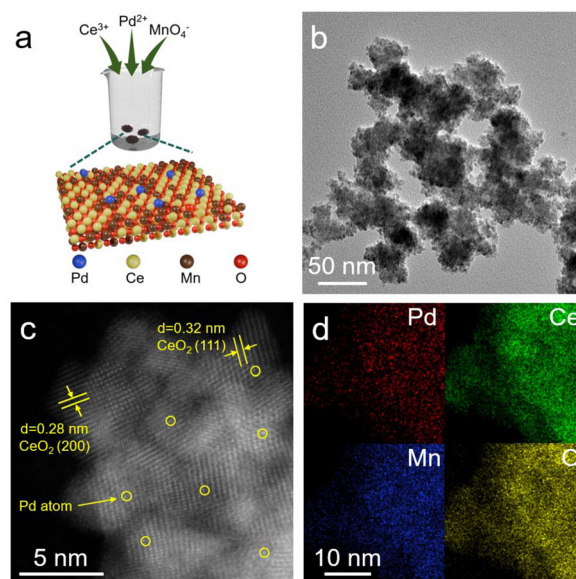

Fig. 1 (a) Schematic illustration of the Pd/CeMn-AR synthesis process. (b) TEM image of Pd/CeMn-AR. (c) HAADF-STEM image of Pd/CeMn-AR. (d) EDX-mapping images of Pd/CeMn-AR.

persion of Pd in Pd/CeMn-AR. We further prepared comparison samples with a similar Pd content *via* a conventional co-precipitation method (Pd/CeMn-CP), impregnation (Pd/CeO_2) and a hydrothermal method (Pd/MnO_x); see the detailed synthesis procedure in the ESI.†[31] Fig. S2–S4† show the HAADF-STEM images and EDX mapping images of these three comparison samples, exhibiting a similar particle size and elemental distribution to those of Pd/CeMn-AR.

Next, powder X-ray diffraction (XRD) was employed to investigate the phase composition of various catalysts. In the XRD pattern in Fig. 2a, both Pd/CeMn-AR and Pd/CeMn-CP samples
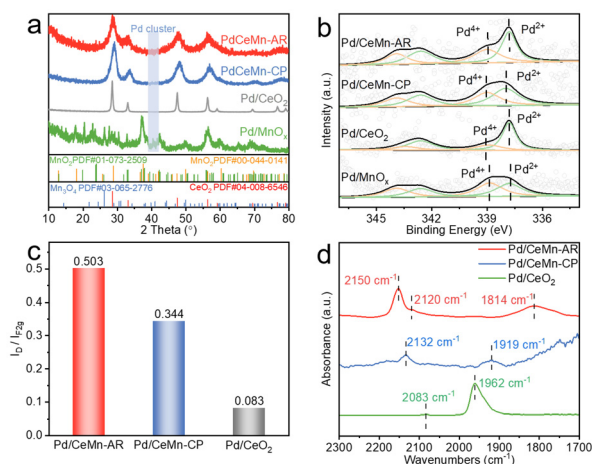

Fig. 2 (a) XRD patterns of Pd/CeMn-AR, Pd/CeMn-CP, Pd/CeO_2 and Pd/MnO_x. (b) Pd 3d XPS spectra of Pd/CeMn-AR, Pd/CeMn-CP, Pd/CeO_2 and Pd/MnO_x. (c) Raman peak ratio (I_D and I_{F2g}) of Pd/CeMn-AR, Pd/CeMn-CP and Pd/CeO_2. (d) *In situ* CO-DRIFTS spectra of Pd/CeMn-AR, Pd/CeMn-CP, and Pd/CeO_2.

show broad diffraction peak positions at $2\theta = 28.5°$, $33.0°$, $47.4°$, $56.4°$, $70°$ and $77.7°$, which can be attributed to the cubic fluorite structure of CeMn solid solutions, consistent with previous studies.[32–34] In the pattern of Pd/MnO$_x$, the peaks at $12.8°$, $19.9°$, $32.7°$ and $56.45°$ correspond to the MnO$_2$ phase (PDF #01-073-2509). The diffraction peaks situated at $2\theta = 18.1°$, $25.7°$, $28.8°$, $37.5°$, $41.9°$, $49.8°$, $60.3°$, $65.1°$ and $69.7°$ can be assigned to the MnO$_2$ phase of MnO$_x$ (PDF #00-044-0141), and the diffraction peaks at $2\theta = 14.3°$, $21.7°$, $26.1°$, $28.9°$ and $43.9°$ can be assigned to the Mn$_3$O$_4$ phase of MnO$_x$ (PDF #03-065-2776). It is noteworthy that the absence of diffraction peaks associated with Pd nanoparticles or palladium oxides in all samples indicates a high dispersion of Pd element, aligning with our TEM observations.[30]

We further conducted X-ray photoelectron spectroscopy (XPS) to obtain detailed electronic information on each catalyst. Fig. 2b shows the fitting results of Pd 3d XPS spectra, where all samples show two sets of peaks at 338 eV and 338.9 eV corresponding to Pd^{2+} and Pd^{4+}, suggesting that the Pd atoms are not aggregated to nanoparticles.[35–39] This proves that Pd on the surface of various samples exists as single atoms. Fig. S5† shows the fitting results of the Mn 3d XPS spectra, where the peaks at 641 eV, 642.4 eV and 644.5 eV are attributed to Mn^{2+}, Mn^{3+} and Mn^{4+}.[40–42] Fig. S6† shows the fitting results of Ce 3d XPS spectra, where the peaks from 882.5 eV to 898.4 eV represent the spin-coupled orbitals of Ce 3d$_{3/2}$, and the peaks from 900.5 eV to 917 eV represent the spin-coupled orbitals of Ce 3d$_{5/2}$. The peaks at 884.1 eV and 903.5 eV represent Ce^{3+}.[38] Previous studies indicate that elevated Ce^{3+} concentrations induce more oxygen vacancies on Ce–Mn solid solution surfaces, thereby improving methane combustion activity.[35,43] The calculated Ce^{3+} ratios of Pd/CeMn-AR, Pd/CeMn-CP and Pd/CeO$_2$ are 19.94%, 15.20%, and 14.97%. It shows that Pd/CeMn-AR prepared using an auto-redox method has more low-valent Ce species, which is favourable for the methane combustion reaction to proceed. Fig. S7† shows the fitting results of the O 1s XPS spectra of different catalysts, where the peaks at 529.7 eV, 531.9 eV and 533.2 eV represent lattice oxygen (O$_{latt}$), defective oxygen (O$_{def}$) and weakly bound oxygen (O$_{OH}$). The concentration of oxygen vacancies can be calculated using O$_{def}$/(O$_{latt}$ + O$_{def}$ + O$_{OH}$),[44] and the order of the percentage of oxygen vacancies is Pd/CeMn-AR > Pd/CeMn-CP > Pd/CeO$_2$. This suggests that more oxygen vacancies can be produced by the auto-redox method. Table S1† lists the proportion of different valence states of each element species for all catalysts, as determined by XPS. Then, Raman measurements were carried out to identify the oxygen vacancy content of various samples. Fig. S8† shows that the primary bonds observed at 450 cm^{-1} belong to the typical F$_{2g}$ mode of the CeO$_2$ fluorite structure.[38] The faint bands at 633 cm^{-1} are attributed to the defect-induced mode (D-mode), relating to the oxygen vacancies.[45] Fig. 2c shows the calculated results of these two Raman bond intensities (I_D/I_{F2g}) in each sample;[37] the oxygen vacancy content follows the sequence: Pd/CeMn-AR > Pd/CeMn-CP > Pd/CeO$_2$. We also used electron paramagnetic resonance (EPR) to measure the oxygen vacancy content of

various samples. Fig. S9† shows the $g = 2.003$ signal corresponding to oxygen vacancy-trapped unpaired electrons in all catalysts, with intensity following Pd/CeMn-AR > Pd/CeMn-CP > Pd/CeO$_2$, indicating the highest oxygen vacancy concentration in Pd/CeMn-AR. This is consistent with our Raman and XPS results, proving that the auto-redox synthesis strategy of Pd/CeMn-AR produces more oxygen vacancies, thereby enhancing methane combustion activity.

We then utilized *in situ* diffuse reflectance infrared Fourier-transform spectroscopy (DRIFTS) to investigate the presence of Pd species in all samples (Fig. 2d). Based on the strong interaction between d-orbital electrons of noble metals and carbon monoxide (CO) molecules, CO-DRIFTS can effectively probe the existing state of Pd centres. For Pd/CeMn-AR, the distinctive peak at 2150 cm^{-1} corresponds to CO adsorption on Ce^{3+},[46] while a weak peak at 2120 cm^{-1} is attributed to the linear adsorption on Pd single atoms.[37] A similar CO linear adsorption peak at 2132 cm^{-1} is also observed for Pd/CeMn-CP, confirming the atomically dispersed character of Pd species. However, the signals corresponding to CO bridge adsorption on Pd nanoparticles are present in both samples within the range of 1800 to 1970 cm^{-1}. The signal for Pd/CeO$_2$ exhibits a comparable trend to those of Pd/CeMn-AR and Pd/CeMn-CP.[37,46] This observation aligns with previous studies on Pd single-atom catalysts, suggesting that it may be due to the mobility of Pd atoms in the CO environment during testing.[46] Combined with TEM, EDX, XRD, XPS, and CO-DRIFTS results, we believe that Pd is dispersed on CeMn solid solutions in the form of single atoms. The nitrogen adsorption–desorption isotherms in Fig. S10† showed negligible differences in the surface areas of Pd/CeMn-AR and Pd/CeMn-CP (196 and 151 m^2 g^{-1}), indicating that the surface area is not a factor affecting the performance.

Catalytic performance evaluation

The methane combustion reaction was evaluated in a fixed-bed reactor with a weight hourly space velocity (WHSV) of 30 000 mL g$_{cat}^{-1}$ h^{-1}. As shown by the catalytic performance in Fig. 3a, the conversion of methane increases with the rise in reaction temperature. Among various samples, Pd/CeMn-AR shows the best low-temperature performance, with the T_{50} reaching 440 °C and the T_{90} reaching 543 °C, which were 82 °C and 84 °C lower than those of its typical Pd/CeO$_2$ counterpart, respectively. The Pd/CeMn-CP catalyst shows the second best low-temperature performance, reaching a T_{50} of 452 °C and T_{90} of 557 °C. This observation not only indicates that CeMn solid solution supports are more advantageous than pure CeO$_2$, but also highlights the significant influence of the preparation methodology on methane combustion performance. Additionally, to demonstrate the superiority of the one-pot synthesis approach, CeMn solid solution supports decorated with Pd single atoms were prepared *via* a similar redox reaction and impregnation procedure (namely, CeMn-AR-Pd), as shown in Fig. S11.† As shown in the catalytic results in Fig. S12,† the methane conversion of CeMn-AR-Pd reaches only 77% at 550 °C, significantly lower than that of Pd/CeMn-AR. We sub-
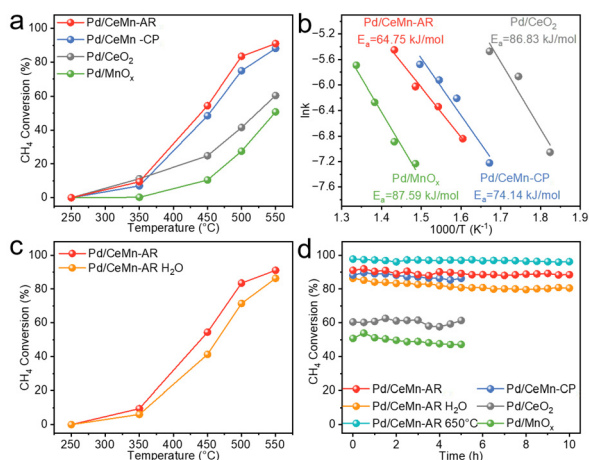
Fig. 3 (a) Catalytic activities for methane oxidation of Pd/CeMn-AR, Pd/CeMn-CP, Pd/CeO$_2$ and Pd/MnO$_x$. (b) Corresponding Arrhenius plots. (c) Effect of the presence of water vapour on the catalytic activity of Pd/CeMn-AR. (d) Long-term stability of Pd/CeMn-AR, Pd/CeMn-CP, Pd/CeO$_2$, Pd/MnO$_x$ and PdCeMn-AR-H$_2$O at 550 °C and 650 °C. The space velocity was set at 30 000 mL g$_{cat}$$^{-1}$ h^{-1}. The feed gas was composed of 0.5% CH$_4$, 20% O$_2$, and balance Ar.

sequently investigated the compositional effect in the ternary system by verifying the feeding ratio of Ce, Mn, and Pd precursors, as shown in Fig. S13.† At a constant Pd loading of 1 wt%, the optimal methane combustion performance of the catalyst was achieved when the Ce : Mn molar ratio was 2 : 1. On this basis, further variations in the Pd loading led to decreased catalytic performance. When evaluating the space velocities, the methane conversion rate gradually decreases, as shown in Fig. S14.†

We then carried out a kinetic study across all samples, while maintaining the methane conversion below 15%.[47] The calculated apparent activation energies (E_a) in Fig. 3b reveal that Pd/CeMn-AR has the lowest energy barrier of 64.75 kJ mol^{-1}, indicating a fast kinetic process. Considering that water resistance is also a key performance indicator for methane combustion catalysts, we incorporated 1.5% water vapor and evaluated the performance of Pd/CeMn-AR. As depicted in Fig. 3c, Pd/CeMn-AR maintained a high activity under wet conditions, with T_{50} at 464 °C and T_{90} at 562 °C, suggesting substantial application potential. Fig. 3d presents the long-term stability measurements of each sample. As expected, the stability of all single-atom samples is satisfactory. For Pd/CeMn-AR, nearly 97% of the original activity remained after 10 hours of continuous catalysis at 550 °C. At the same reaction time and temperature, as much as 98% of initial methane conversion remained under wet conditions. Furthermore, a comparative sample of CeO$_2$-supported Pd particles was prepared (namely, Pd$_{NP}$/CeO$_2$). As shown in Fig. S15 and S16,† although it exhibits better activity compared to Pd$_{NP}$/CeO$_2$ in the low-temperature region, its conversion rapidly declines above 500 °C. Stability tests revealed that its activity decayed by 19% within the first 30 minutes and it retained only 74% of the initial

activity after 2 hours. This result highlights the crucial role of stable single-atom Pd active centers in methane combustion at elevated temperatures. Fig. S17–S19 and Table S2† list the detailed structural characterization of the reacted samples. No significant Pd nanoparticle agglomeration was observed in the high-resolution TEM image, and the corresponding EDX mapping images showed that the Pd is uniformly distributed through the CeMn support. The XRD patterns of the used samples were consistent with those prior to the reaction. The above results confirm the catalyst's robust structural stability. Compared to the existing Pd-based single-atom catalysts for methane combustion, our Pd/CeMn-AR catalyst exhibits a decreased reaction temperature, faster kinetic process, enhanced structural stability, and improved atom utilization efficiency (Table S3†).

Mechanism investigation

To investigate the factors underlying the performance disparities among various samples, CH$_4$ and O$_2$ temperature programmed desorption (TPD) tests were carried out to examine the adsorption ability of various catalysts on both substrates. From the CH$_4$-TPD profile in Fig. 4a, the peaks located at 200 °C are attributed to weak CH$_4$ adsorption. The peaks located at 391 °C and 575 °C are attributed to medium CH$_4$ adsorption. Compared to those of pure CeO$_2$ and MnO$_x$, the methane adsorption characteristics of both Pd/CeMn-AR and Pd/CeMn-CP exhibit an optimized state: the weak adsorption is enhanced, while the strong adsorption is weakened, and medium adsorption occurs. Previous studies have pointed out that medium methane adsorption is most efficient for methane activation, which explains the preference of CeMn solid solutions over CeO$_2$ and MnO$_x$. The O$_2$-TPD results in Fig. 4b can be divided into three regions: weakly bound
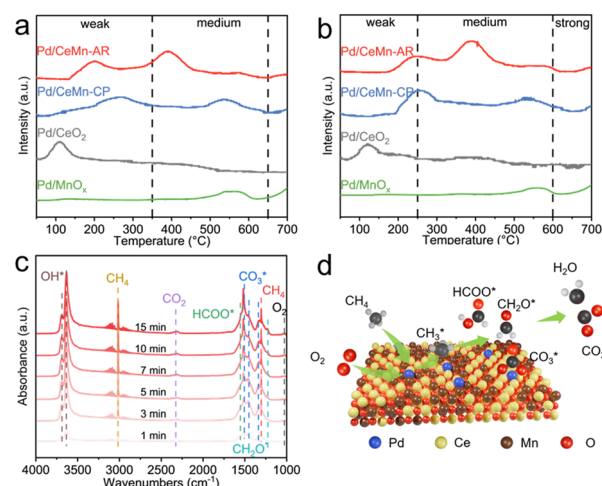

Fig. 4 (a) CH$_4$-TPD profiles and (b) O$_2$-TPD profiles of Pd/CeMn-AR, Pd/CeMn-CP, Pd/CeO$_2$ and Pd/MnO$_x$. (c) *In situ* DRIFTS for methane oxidation over the Pd/CeMn-AR catalyst at 550 °C. Test conditions: 0.5% CH$_4$, 20% O$_2$, and balance Ar. (d) Schematic diagram of the reaction mechanism of CH$_4$ and O$_2$ on the catalyst surface.

surface oxygen species (below 250 °C), active oxygen species adsorbed on oxygen vacancies (from 250 °C to 600 °C), and bulk oxygen species (above 600 °C).[20,48] Compared to Pd/CeMn-CP, Pd/CeO$_2$ and Pd/MnO$_x$, Pd/CeMn-AR exhibits the strongest oxygen desorption ability within the second region and presents an additional desorption peak at 393 °C, indicating a higher concentration of oxygen vacancies, which is advantageous for methane combustion. Notably, such robust O$_2$ desorption behavior was not found in the O$_2$-TPD profiles of CeMn-AR-Pd in Fig. S20,† highlighting the significance of the one-pot synthesis method in preserving oxygen vacancies on the catalyst surface.

To elucidate the methane conversion process, we recorded the *in situ* DRIFTS spectra in the reaction gas at 550 °C. As shown in Fig. 4c, the signals of the reaction substrates, intermediates and products appeared in the spectra, as the reaction gas was continuously passed. Bands corresponding to the OH stretching vibration (3736 cm^{-1} and 3536 cm^{-1}), gaseous methane (3054 cm^{-1} and 2956 cm^{-1}), and gaseous CO$_2$ (2286 cm^{-1} and 2384 cm^{-1}) appeared in the first minute, indicating a rapid combustion process.[20,49,50] In line with prior investigations, both formate (1588 cm^{-1} and 1545 cm^{-1}) and carbonate (1340 cm^{-1} and 1540 cm^{-1}) species were detected throughout the measurement procedure, implying a sluggish intermediate-to-product conversion process.[20,38,51] In contrast, the absorption bands belonging to the CH$_2$O* intermediate (1225 cm^{-1}) appeared only after 7 min, suggesting a fast dehydrogenation process of CH$_2$O* to HCOO*.[38] Therefore, a possible reaction mechanism of methane conversion on Pd/CeMn-AR is proposed in Fig. 4d. Initially, methane molecules are activated and form CH$_x$* species at the Pd site. Subsequently, the surface lattice oxygen of the CeMn support participates in the reaction and oxidizes CH$_3$* to form CH$_2$O*. CH$_2$O* species interact with OH* or the lattice oxygen on the surface to form carbonate species (CO$_3$*) and formate species (HCOO*). These intermediates are further oxidized on the catalyst surface, yielding CO$_2$ and H$_2$O.[18,51,52] Finally, oxygen molecules from the substrate are captured by oxygen vacancies on the support, completing the catalytic cycle.

Conclusions

In summary, we successfully synthesized a CeMn solid solution-loaded Pd single atom catalyst *via* a modified auto-redox reaction. Pd/CeMn-AR exhibited superior methane combustion performance, especially at elevated temperatures. The T_{90} of Pd/CeMn-AR is only 543 °C, significantly lower than those of Pd/CeO$_2$ (627 °C), Pd/MnO$_x$ (634 °C) and Pd/CeMn-CP (557 °C). Furthermore, Pd/CeMn-AR showed only a 5% decrease of its initial activity after 10 hours of long-term stability testing. Systematic characterization and mechanism studies reveal that the abundant surface oxygen vacancies not only facilitate the adsorption of methane and oxygen molecules but also accelerate the oxidative conversion of CH$_3$* intermediates. This work presents a convenient but efficient

synthesis procedure for creating highly dispersed active centers and abundant defects, thereby enhancing catalytic activity. We anticipate that the proposed strategy based on the auto-redox reaction will find widespread application in various catalyst designs and contribute to other sustainable catalytic systems.

Data availability

The data supporting this article have been included as part of the ESI.†

Conflicts of interest

There are no conflicts to declare.

Acknowledgements

References

1 X. B. Feng, J. Lei, D. Y. Li, S. P. Tian, Z. Xing, W. Hua, C. He and K. Z. Li, *J. Energy Chem.*, 2022, **75**, 173–215.

2 H. G. Peng, C. Rao, N. Zhang, X. Wang, W. M. Liu, W. T. Mao, L. Han, P. F. Zhang and S. Dai, *Angew. Chem., Int. Ed.*, 2018, **57**, 8953–8957.

3 K. Murata, Y. Mahara, J. Ohyama, Y. Yamamoto, S. Arai and A. Satsuma, *Angew. Chem., Int. Ed.*, 2017, **56**, 15993–15997.

4 R. J. Farrauto, *Science*, 2012, **337**, 659–660.

5 S. Yasumura, K. Nagai, S. Miyazaki, Y. C. Qian, D. T. Chen, T. Toyao, Y. Kamiya and K. I. Shimizu, *J. Am. Chem. Soc.*, 2024, **146**, 20982–20988.

6 E. D. Goodman, A. S. Asundi, A. S. Hoffman, K. C. Bustillo, J. F. Stebbins, S. R. Bare, S. F. Bent and M. Cargnello, *Adv. Mater.*, 2021, **33**, 2104533.

7 M. Cargnello, J. J. D. Jaén, J. C. H. Garrido, K. Bakhmutsky, T. Montini, J. J. C. Gámez, R. J. Gorte and P. Fornasiero, *Science*, 2012, **337**, 713–717.

8 B. Yuan, T. Zhu, B. Nie, X. Zhang, Y. Han, M. Wang, C. Li and X. Zhang, *J. Environ. Chem. Eng.*, 2024, **12**, 113860.

9 X. Huang, W. Yang and J. Li, *Processes*, 2024, **12**, 1630.

10 L. M. Toscani, P. A. Curyk, M. G. Zimicz, E. B. Halac, M. E. Saleta, D. G. Lamas and S. A. Larrondo, *Appl. Catal., A*, 2019, **587**, 117235.

11 X. Y. Li, Y. X. Liu, J. G. Deng, S. H. Xie, X. T. Zhao, Y. Zhang, K. F. Zhang, H. Arandiyan, G. S. Guo and H. X. Dai, *Appl. Surf. Sci.*, 2017, **403**, 590–600.

12 Y. H. Xiao, W. T. Zhao, K. Zhang, Y. Y. Zhang, X. Y. Wang, T. H. Zhang, X. W. Wu, C. Q. Chen and L. L. Jiang, *Dalton Trans.*, 2017, **46**, 16967–16972.

13 B. Yue, R. Zhou, X. Zheng and W. Lu, *Fuel Process. Technol.*, 2008, **89**, 728–735.

14 A. J. Zarur and J. Y. Ying, *Nature*, 2000, **403**, 65–67.

15 Y. Wang, H. Arandiyan, H. A. Tahini, J. Scott, X. Tan, H. X. Dai, J. D. Gale, A. L. Rohl, S. C. Smith and R. Amal, *Nat. Commun.*, 2017, **8**, 15553.

16 X. L. Feng, D. P. Liu, B. L. Yan, M. Z. Shao, Z. M. Hao, G. B. Yuan, H. H. Yu and Y. Zhang, *Angew. Chem., Int. Ed.*, 2021, **60**, 18552–18556.

17 X. L. Feng, X. R. Gong, D. P. Liu, Y. Li, Y. Jiang and Y. Zhang, *Angew. Chem., Int. Ed.*, 2023, **62**, e202313068.

18 Z. Y. Tang, T. Zhang, D. C. Luo, Y. J. Wang, Z. Hu and R. T. Yang, *ACS Catal.*, 2022, **12**, 13457–13474.

19 H. M. Duan, F. X. Kong, X. Z. Bi, L. Chen, H. T. Chen, D. J. Yang and W. X. Huang, *ACS Catal.*, 2024, **14**, 17972–17992.

20 J. Tao, H. Lin, J. Deng, Y. Liu, L. Jing, Z. Hou, L. Wei, Z. Wang and H. Dai, *Appl. Catal., B*, 2025, **360**, 124554.

21 M. Cargnello, T. Montini, S. Polizzi, N. L. Wieder, R. J. Gorte, M. Graziani and P. Fornasiero, *Dalton Trans.*, 2010, **39**, 2122–2127.

22 N. F. Wang, S. Q. Li, Y. C. Zong and Q. Yao, *J. Aerosol Sci.*, 2017, **105**, 64–72.

23 F. Niu, S. Q. Li, Y. C. Zong and Q. Yao, *J. Phys. Chem. C*, 2014, **118**, 19165–19171.

24 W. W. Yang, F. Polo-Garzon, H. Zhou, Z. N. Huang, M. F. Chi, H. Meyer III, X. B. Yu, Y. Y. Li and Z. L. Wu, *Angew. Chem., Int. Ed.*, 2023, **62**, e202217323.

25 Y. Ozawa, Y. Tochihara, M. Nagai and S. Omi, *Catal. Commun.*, 2003, **4**, 87–90.

26 G. Groppi, C. Cristiani, L. Lietti, C. Ramella, M. Valentini and P. Forzatti, *Catal. Today*, 1999, **50**, 399–412.

27 D. Jiang, G. Wan, J. H. Stenlid, C. E. García-Vargas, J. H. Zhang, C. J. Sun, J. R. Li, F. Abild-Pedersen, C. J. Tassone and Y. Wang, *Nat. Catal.*, 2023, **6**, 618–627.

28 T. C. Pu, J. Q. Ding, X. Tang, K. W. Yang, K. Wang, B. Huang, S. Dai, Y. He, Y. Shi and P. F. Xie, *ACS Appl. Mater. Interfaces*, 2022, **14**, 43141–43150.

29 X. Wang, Y. B. Zhang, S. Y. Song, X. G. Yang, Z. Wang, R. C. Jin and H. J. Zhang, *Angew. Chem., Int. Ed.*, 2016, **55**, 4542–4546.

30 K. Qi, J. L. Xie, Z. Zhang, D. Fang, D. Han, X. Q. Liu, P. J. Gong, F. X. Li and F. He, *Powder Technol.*, 2018, **338**, 774–782.

31 M. Liu, S. Hu, Y. Zhang, C. Zhao, W. Jiang, C. Qi, X. Zhu, P. Qiu, Y. Sun, K. Kato, Y. Zhao, X. Li, M. Yamauchi and W. Luo, *Adv. Mater. Interfaces*, 2021, **8**, 2002060.

32 L. M. Shi, W. Chu, F. F. Qu, J. Y. Hu and M. M. Li, *J. Rare Earths*, 2008, **26**, 836–840.

33 Y. J. Luo, D. F. Lin, Y. B. Zheng, X. S. Feng, Q. H. Chen, K. Zhang, X. Y. Wang and L. L. Jiang, *Appl. Surf. Sci.*, 2020, **504**, 144481.

34 E. Y. Liberman, B. S. Kleusov, E. A. Simakina, T. V. Kon'kova, V. N. Grunskii, A. D. Stoyanova and A. V. Denisenko, *Russ. J. Appl. Chem.*, 2023, **96**, 156–161.

35 L. X. Jia, L. L. Zhang, H. L. Wang, X. Wang, S. Y. Song and H. J. Zhang, *ChemCatChem*, 2024, **16**, e202401251.

36 X. X. Han, L. L. Zhang, R. Zhang, K. Wang, X. Wang, B. Li, Z. P. Tao, S. Y. Song and H. J. Zhang, *Dalton Trans.*, 2024, **53**, 3290–3295.

37 H. Zhao, Y. L. Tan, L. Li, Y. Su, A. Q. Wang, X. Y. Liu and T. Zhang, *Chem. Eng. J.*, 2023, **451**, 138937.

38 M. W. Wu, M. Miao, W. Z. Li, X. Zhang, L. L. Zhang, T. M. Zhen, Y. Fu, J. T. Jin and L. Yuan, *Fuel*, 2023, **331**, 125575.

39 L. Li, S. T. Xue, M. J. Wei, H. Yao, Y. Dai and Z. Y. Fei, *Appl. Surf. Sci.*, 2022, **599**, 153909.

40 B. Chutia, N. Hussain, P. Puzari, D. Jampaiah, S. K. Bhargava, E. V. Matus, I. Z. Ismagilov, M. Kerzhentsev and P. Bharali, *Energy Fuel*, 2021, **35**, 10756–10769.

41 J. Q. Yang, H. Deng, Y. Q. Lu, J. Z. Ma, W. P. Shan and H. He, *Ind. Eng. Chem. Res.*, 2023, **62**, 8665–8672.

42 G. Liu, L. Sun, J. H. Liu, F. Wang and C. J. Guild, *Mol. Catal.*, 2017, **440**, 148–157.

43 J. R. Wang, D. W. Liu, W. X. Zhang, B. Hou, Y. Deng, X. X. Ma and L. Xu, *ChemCatChem*, 2024, **16**(9), e202301768.

44 J. K. Zhang, Y. Men, Y. M. Wang, L. N. Liao, S. Liu, J. G. Wang and W. An, *Int. J. Hydrogen Energy*, 2024, **51**, 1185–1199.

45 H. Zhao, L. C. Bian, J. C. Du and Y. K. Zhao, *Dalton Trans.*, 2022, **51**, 18562–18571.

46 L. A. Zhang, S. L. Wan, C. C. Du, Q. Wan, H. Pham, J. F. Zhao, X. Y. Ding, D. Y. Wei, W. Zhao, J. W. Li, Y. P. Zheng, H. Xie, H. Zhang, M. S. Chen, K. H. L. Zhang, S. Wang, J. D. Lin, J. Y. Huang, S. Lin, Y. Wang, A. K. Datye, Y. Wang and H. F. Xiong, *Nat. Commun.*, 2024, **15**, 1234.

47 H. L. Wang, M. S. Bootharaju, J. H. Kim, Y. Wang, K. Wang, M. Zhao, R. Zhang, J. Xu, T. Hyeon, X. Wang, S. Y. Song and H. J. Zhang, *J. Am. Chem. Soc.*, 2023, **145**, 2264–2270.

48 H. C. Yao and Y. F. Y. Yao, *J. Catal.*, 1984, **86**, 254–265.

49 P. F. Qu, S. L. Wang, W. Hu, Y. Wu, J. J. Chen, G. C. Zhang, P. Q. Shen, Y. Q. Chen and L. Zhong, *Catal. Commun.*, 2020, **135**, 105900.

50 J. Y. Cai, S. H. Wu, M. M. Liu, Y. Zhang, M. Wang, Y. Liu, Y. B. Yu and W. P. Shan, *Appl. Catal., B*, 2025, **361**(13), 124559.

51 J. S. Tian, R. Kong, Z. Wang, L. Fang, T. Y. He, D. Jiang, H. G. Peng, T. L. Sun, Y. H. Zhu and Y. Wang, *ACS Catal.*, 2023, **14**, 183–191.

52 S. Y. Chen, S. D. Li, R. Y. You, Z. Y. Guo, F. Wang, G. X. Li, W. T. Yuan, B. E. Zhu, Y. Gao, Z. Zhang, H. S. Yang and Y. Wang, *ACS Catal.*, 2021, **11**, 5666–5677.